Organic Geochemistry 116 (2018) 90–102

Contents lists available at ScienceDirect

Organic Geochemistry

journal homepage: www.elsevier.com/locate/orggeochem

Distribution and export of isoprenoid tetraether lipids in suspended particulate matter from the water column of the Western Atlantic Ocean

Sarah J. Hurley [a,*,1], Julius S. Lipp [b], Hilary G. Close [c,2], Kai-Uwe Hinrichs [b], Ann Pearson [a,*]

[a] Department of Earth and Planetary Sciences, Harvard University, Cambridge, MA 02138, USA
[b] Organic Geochemistry Group, MARUM – Center for Marine Environmental Sciences & Department of Geosciences, University of Bremen, Bremen 28359, Germany
[c] Department of Geology and Geophysics, University of Hawaii, Honolulu, HI 96822, USA

ARTICLE INFO

Article history:
Received 5 April 2017
Received in revised form 14 November 2017
Accepted 15 November 2017
Available online 22 November 2017

Keywords:
GDGT
Export
TEX_{86}
Suspended particulate matter
Intact polar lipids

ABSTRACT

The TEX_{86} paleotemperature proxy is based on the distribution of archaeal glycerol dibiphytanyl glycerol tetraether (GDGT) lipids preserved in marine sediments, yet both the influence of different physiological factors on the structural distribution of GDGTs and the mechanism(s) by which GDGTs is(are) exported to marine sediments remain(s) unresolved. We investigated the abundance and structural distribution of GDGTs in the South-west and Equatorial Atlantic Ocean in four water column profiles spanning 48 degrees of latitude. The depth distribution was consistent with production by ammonia-oxidizing Thaumarchaeota; maximum GDGT concentration occurred at the base of the NO_2^- maximum, core GDGTs dominated the structural distribution in surface waters above the NO_2^- maximum, and intact polar GDGTs – potentially indicating live cells – were more abundant below the NO_2^- maximum. Between 0 and1000 m, > 98% of the integrated GDGT inventory was present in waters at and below the NO_2^- maximum. Depth profiles of TEX_{86} temperature values displayed local minima at the NO_2^- maximum, while the ratio of GDGT-2:GDGT-3 increased with depth. A model based on the results predicts an average depth of origin for GDGTs exported to sediments between ca. 80–250 m. In the model, exported TEX_{86} values are remarkably insensitive to change in the average depth of origin of GDGTs. However, TEX_{86} values exported from the water column appear to reflect euphotic zone productivity, possibly due to the correlative intensity of organic matter remineralization providing substrates for ammonia oxidation. Predicting the influence of these regional controls on sedimentary TEX_{86} records requires a better understanding of the interaction between GDGT production, particle dynamics, and the depth of origin for exported organic matter.

1. Introduction

Archaeal glycerol dibiphytanyl glycerol tetraether (GDGT) lipids (Supplementary Fig. 1) are ubiquitous in marine sediments and form the basis of the TEX_{86} sea surface temperature (SST) proxy (Schouten et al., 2002). GDGTs in the water column are thought to be sourced primarily from ammonia-oxidizing archaea (AOA) affiliated with the phylum Thaumarchaeota (formerly Marine Group I Crenarchaeota; Brochier-Armanet et al., 2008; Spang et al., 2010). AOA perform the first and rate-limiting step in nitrification, the oxidation of NH_4^+ to NO_2^-, catalyzed by the archaeal ammonia monooxygenase enzyme, *amoA* (Könneke et al., 2005). Accordingly, maximum Thaumarchaeota cell numbers, as well as maximum copies of *amoA* and 16S rRNA genes, occur with the primary NO_2^- maximum near the base of the euphotic zone (Massana et al., 1997; Murray et al., 1999; Karner et al., 2001; Francis et al., 2005; Church et al., 2010; Santoro et al., 2010; Smith et al., 2016). GDGT concentration mirrors the trend in overall thaumarchaeal abundance, with low concentration in surface waters and a maximum concentration near the base of the euphotic zone (Sinninghe Damsté et al., 2002; Turich et al., 2007; Schouten et al., 2012; Basse et al., 2014; Lincoln et al., 2014; Xie et al., 2014; Kim et al., 2016).

Thaumarchaeota produce GDGTs containing from zero to four cyclopentane rings (GDGT-0 to GDGT-4) or four cyclopentane rings and one additional cyclohexane ring (e.g. in crenarchaeol; Sinninghe Damsté, 2002; Supplementary Fig. 1). The ratio between

* Corresponding authors.
E-mail addresses: sarah.hurley@colorado.edu (S.J. Hurley), pearson@eps.harvard.edu (A. Pearson).
[1] Current address: Department of Geological Sciences, University of Colorado Boulder, Boulder, CO 80309, USA.
[2] Current address: Rosenstiel School of Marine and Atmospheric Science, University of Miami, Miami, FL 33149, USA.

https://doi.org/10.1016/j.orggeochem.2017.11.010
0146-6380/

GDGTs with one to three cyclizations and the crenarchaeol regioisomer is the basis of the TEX_{86} temperature proxy. TEX_{86} is theoretically based on the concept of homeoviscous membrane adaptation, in which an organism regulates membrane fluidity in response to physical or chemical perturbations (e.g. by incorporation of cyclization in response to increasing temperature). However, TEX_{86} is empirically calibrated using a correlation between the distribution of select GDGT structures in marine sediments and sea surface temperature or subsurface (0–200 m) temperature (Schouten et al., 2002; Kim et al., 2010; Tierney and Tingley, 2015).

Modern TEX_{86} core-top calibrations generally predict SST to within ± 3–5 °C (Kim et al., 2010; Tierney and Tingley, 2014). TEX_{86} paleoclimate records span temporally and geographically diverse events in Earth history, including the Last Glacial Maximum (Huguet et al., 2006b), the Paleocene-Eocene Thermal Maximum PETM (Zachos et al., 2006) and Cretaceous Ocean Anoxic Events (Schouten et al., 2003). TEX_{86} provides an alternative to proxies that cannot be applied for sediments older than the Paleogene (e.g. $U^{k'}_{37}$), or when dissolution or diagenetic processes have impacted the preservation of carbonate-based geochemical signatures (Schouten et al., 2013).

The TEX_{86} proxy rests on the assumptions that temperature is the dominant factor driving lipid composition in planktonic Thaumarchaeota, and that this signal is ultimately preserved in marine sediments. Mesophilic culture and mesocosm studies show that GDGT cyclization can increase at higher temperature (Wuchter et al., 2004; Schouten et al., 2007; Elling et al., 2015; Qin et al., 2015). However, suspended material filtered from the marine water column has TEX_{86} values that do not consistently reflect in situ temperature (Wuchter et al., 2005; Ingalls et al., 2006; Turich et al., 2007; Schouten et al., 2012; Basse et al., 2014; Hernández-Sánchez et al., 2014; Xie et al., 2014; Zhu et al., 2016). In fact, calculated TEX_{86} values often reach a maximum below 200 m, yielding thermocline and sub-thermocline temperatures greater than local sea surface temperatures (Schouten et al., 2012; Basse et al., 2014; Xie et al., 2014; Kim et al., 2016). Therefore, variables other than surface or shallow subsurface temperatures appear to be important additional factors in determining water column TEX_{86} signals.

Recent culture work reveals that ammonia oxidation rate can be a temperature-independent influence on GDGT cyclization in the model thaumarchaeon *Nitrosopumilus maritimus* SCM1 (Hurley et al., 2016). This finding reconciles similar culture experiments with *N. maritimus* that have identified growth stage (Elling et al., 2014) and O_2 availability (Qin et al., 2015) as variables affecting TEX_{86}. In cultures of *N. maritimus*, TEX_{86} correlated negatively with ammonia oxidation rate, resulting in warmer TEX_{86} values at slower oxidation rates and colder values at faster oxidation rates (Hurley et al., 2016). This relationship provides an explanation for why warm upper water columns with lower rates of both primary production and sub-photic zone nutrient regeneration, i.e. lower ammonia oxidation rate, have in situ TEX_{86} temperature values that are too high (e.g. Wuchter et al., 2005), whereas warm upper water columns in high-nutrient upwelling zones have apparent in situ TEX_{86} temperature values that are too low (e.g. Xie et al., 2014).

In order to better understand the environmental factors influencing TEX_{86}, we have examined GDGT distributions in two particle size classes, 0.3–0.7 μm and 0.7–53 μm, between 0 and 1000 m along a transect in the South-west and Equatorial Atlantic Ocean (ca. 40°S to 10°N). We relate the abundance and structural distribution of GDGTs to water column properties. We then model different scenarios to explore how the depth of GDGT export affects the proxy ratio exported to marine sediments.

2. Methods

2.1. Sampling and lipid extraction

Samples were collected from aboard the R/V Knorr during cruise KN210-04 (Fig. 1) in March–May 2013 from 38.0°S 45.0°W (Station 2), 22.5°S 33.0°W (Station 7), 2.7°S 28.5°W (Station 15) and 9.7°N 55.3°W (Station 23). Suspended particulate matter samples were collected between 0 and 1000 m at each station to increase depth resolution in the upper water column, yet full water column depth ranged from 3762 m at Station 23 to 5110 m at Station 2 (Table 1). Samples for inorganic nutrient analysis were collected in HDPE bottles and frozen (−20 °C) immediately after sample collection. All nutrient data have been deposited in the Biological and Chemical Oceanography (BCO) Data System (Kujawinski and Longnecker, 2013).

The CTD rosette system was equipped with a SBE43 oxygen sensor, a Wet Labs FLNTURTD combination fluorometer and turbidity sensor, and a WetLabs C-star transmissometer (operating at a 660 nm with 25 cm path length). The SBE43 O_2 data were calibrated based on the discrete water samples analyzed during the cruise. Fluorescence values from the WET Labs ECO-AFL/FL were converted from volts to mg/m^3 using calibration values from WETLabs. All CTD data are publically accessible in the BCO Data System (Kujawinski and Longnecker, 2014).

Seawater was sequentially filtered in situ via submersible pumps (WTS-LV 08 upright: McLane Research Laboratories, Inc), with total collected volumes between 710 and 10,518 l (mean 3049 l) per depth. Pumps were equipped with three filter tiers, each 142 mm in diameter. The first tier was fitted with a 53 μm mesh Nitex screen, the second with two (stacked) pre-combusted glass fiber filters (Whatman GF/F; 0.7 μm), and the last two (stacked) pre-combusted glass fiber filters (Sterlitech GF-75; 0.3 μm). Filter size was chosen based on ease of comparison to a typical suspended class of particulate organic matter (0.7–53 μm), while the sub-μm class cut off at 0.3 μm represents the smallest available glass fiber filter extractable with organic solvents. All filters were wrapped in pre-combusted Al foil and frozen immediately at −80 °C after recovery.

Filters were extracted in Teflon vessels in 90:10 CH_2Cl_2:CH_3OH using microwave-assisted extraction with a CEM Mars system. This extraction method was the most efficient way to process all 229 filter samples and is reported to have good performance for water column particles (Huguet et al., 2010). Lipid extraction consisted of two steps: a 30 min ramped heating program to 70 °C with a 20 min hold, after which solvent was decanted and fresh solvent added, and then a 30 min ramped heating program to 100 °C with a 20 min hold. The extracts from the successive extraction steps were combined, concentrated under a stream of ultrapure N_2, and stored at −20 °C until measurement. All lipid data have been deposited in the Pangaea database under the DOI https://doi.pangaea.de/10.1594/PANGAEA.861376.

2.2. Intact polar and core lipid analysis

Intact polar lipids (IPLs) and core lipids were analyzed from a 2–10% aliquot of the TLE in MeOH on a Dionex Ultimate 3000RS ultra high performance liquid chromatography (UHPLC) system connected to an ABSciEX QTRAP4500 Triple Quadrupole/Ion Trap mass spectrometry (MS) instrument equipped with a TurboIonSpray ion source operating in positive electrospray (ESI) mode. Separation of core and intact polar lipids was achieved using reversed phase HPLC with an ACE3 C_{18} column (2.1 × 150 mm × 3 μm; Advanced Chromatography Technologies, Aberdeen, Scotland) maintained at 45 °C (Zhu et al., 2013). Target compounds were detected using

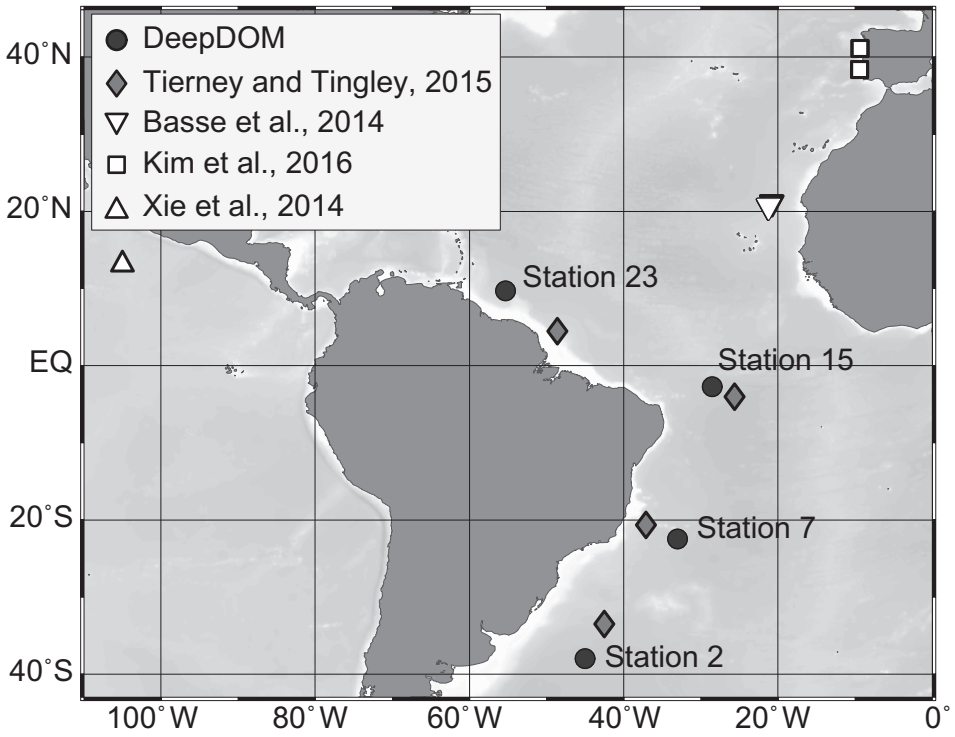

Fig. 1. Locations of sampling stations from the DeepDOM cruise (filled circles; KN210-04 on R/V Knorr, March-May 2013) at 38.0°S 45.0°W (Station 2), 22.5°S 33.0°W (Station 7), 2.7°S 28.5°W (Station 15), and 9.7°N 55.3°W (Station 23). Sediment locations nearest to each DeepDOM station (filled diamonds) at 33.5°S 42.5°W (Location 2a), 20.6°S 37.1°W (Location 7a), 4.0°S 25.6°W (Location 15a), and 4.5°N 48.6°W (Location 23a) are from the surface sediment TEX_{86} database (Tierney and Tingley, 2015). Locations of published SPM datasets used for TEX_{86} profile comparisons: 13°N 105°W (Xie et al., 2014), 21.3°N 20.9°W (Basse et al., 2014), 41.1°N 9.4°W and 38.4°N 9.4°W (Kim et al., 2016).

Table 1
Sediment locations in the surface sediment TEX_{86} database (Tierney and Tingley, 2015) nearest to each sampling station in the South-west and Equatorial Atlantic. The nearest (N) sediment location (Location 23a, Location 15a, Location 7a, and Location 2a) and nearest five (N5) sediment locations were determined by distance matching using the Law of Cosines.

	Distance (km)	TEX_{86}	TEX_{86}^{H} T (°C)	OISSTavg (°C)[a]	[2/3] Ratio
Station 23				27.8	
N (23a)	941	0.65	25.6	27.6	5.73
N5	961 ± 19	0.66 ± 0.05	26.0 ± 2.2	27.7 ± 0.1	5.32 ± 2.17
Station 15				27.2	
N (15a)	352	0.57	22.1	26.9	12.37
N5	501 ± 123	0.59 ± 0.01	22.8 ± 0.5	27.1 ± 0.4	10.28 ± 1.25
Station 7				19.5	
N (7a)	472	0.67	26.5	25.9	5.20
N5	677 ± 141	0.66 ± 0.01	26.1 ± 0.3	25.4 ± 0.4	6.85 ± 1.13
Station 2				17.6	
N (2a)	550	0.54	20.1	19.5	7.38
N5	641 ± 62	0.54 ± 0.01	20.4 ± 0.7	19.5 ± 0.3	6.4 ± 0.98

[a] Optimum interpolation sea SST for each sediment location and sampling site averaged between 1981 and 2011.

scheduled multiple reaction monitoring (sMRM) of diagnostic MS/MS transitions. Ion source, MRM transitions and other MS parameters were optimized by direct infusion or flow injection analysis of total lipid extracts of *N. maritimus*. Lipid quantification was achieved by injecting an internal standard (C_{46}-GTGT; Huguet et al., 2006a). Lipid abundances were corrected for response factors of commercially available, as well as purified, standards as described by Elling et al. (2014).

The TEX_{86} ratio (Eq. 1), TEX_{86} derived-temperature (Eq. 2), and GDGT-2:GDGT-3 ratio ([2/3], Eq. 3) were calculated according to Schouten et al. (2002), Kim et al. (2010) and Taylor et al. (2013), respectively.

$$TEX_{86} = \frac{[\text{GDGT-2}] + [\text{GDGT-3}] + [\text{Cren'}]}{[\text{GDGT-1}] + [\text{GDGT-2}] + [\text{GDGT-3}] + [\text{Cren'}]} \quad (1)$$

$$\text{SST} = 68.4 \times \log(TEX_{86}) + 38.6 \quad (2)$$

$$[2/3] = \frac{\text{GDGT-2}}{\text{GDGT-3}} \quad (3)$$

Total GDGT concentration in each size class was calculated as the sum of GDGTs with hexose- (1G-GDGTs), dihexose- (2G-GDGTs), and hexose-phosphohexose (HPH-GDGTs) head groups, and core GDGTs (C-GDGTs) at each sampling depth. The [2/3] ratio

and TEX_{86} temperature of total GDGTs in each size class were calculated using a mass-weighted average of C-, 1G-, 2G-, and HPH-GDGTs at each sampling depth.

2.3. Sedimentary GDGTs and long term SST data

The sediment locations nearest to each sampling site were gathered from the TEX_{86} surface sediment database (Tierney and Tingley, 2015) by distance matching using the Law of Cosines (Fig. 1). The nearest sediment sites (N) were located 941 km from Station 23 at 4.5°N 48.6°W (Location 23a), 352 km from Station 15 at 4.0°S 25.6°W (Location 15a), 472 km from Station 7 at 20.6°S 37.1°W (Location 7a) and 550 km from Station 2 at 33.5°S 42.5°W (Location 2a) (Table 1; Fig. 1). The five sediment locations nearest to each sampling site were then determined to assess the variability in TEX_{86} and the [2/3] ratio on > 100 km distance scales. The nearest five sediment sites (N5) were 961 ± 19 km from Station 23, 501 ± 123 km from Station 15, 677 ± 141 km from Station 7 and 641 ± 62 km from Station 2 on average. The standard deviation in sedimentary TEX_{86} derived-temperature from the nearest five sediment locations was < 3 °C for each sampling station, while the standard deviation in [2/3] ratio was < 3 (Table 1).

Co-located SST values from sampling and sediment sites were found in the 0.25°×0.25° NOAA daily Optimum Interpolation Sea Surface Temperature (OISST) based on advanced very-high resolution radiometer (AVHRR) measurements (Reynolds et al., 2007). Values for 1981–2011 were averaged (henceforth $OISST_{avg}$) in order to best represent the integrated time period reflected in sediments, and to compare to measured conditions in the water column during the discrete timepoints sampled (Table 1).

3. Results

3.1. Oceanographic setting

The DeepDOM cruise track (Fig. 1) traversed the equatorial and subtropical gyre surface regimes and deep water masses of North Atlantic Deep Water (NADW) and Antarctic Intermediate Water (AAIW). AAIW is centered at a depth of ca. 800 m and is characterized by relatively low salinity and high O_2. AAIW mixes gradually with NADW below and mode water above as it flows northward; its effects were detected strongly at Station 2 and weakly at Station 7. Surface temperature is generally lower at the higher latitudes (20 °C at Station 2) and increases towards the equator (27 °C at Station 7 and 28-29 °C at Stations 15 and 23). The mixed layer shoals near the equator, coincident with higher equatorial productivity and the development of a zone of lower O_2 centered at ca. 400 m depth (between 10°S and 10°N; Supplementary Fig. 2). We analyzed four sampling stations: Station 23 at the edge of the Amazon River plume, Station 15 in the equatorial region, Station 7 in the South Atlantic gyre and Station 2 in the southern subtropical transition zone. At each station, the NO_2^- maximum occurred 5–30 m below the deep chlorophyll maximum (Fig. 2 a; Table 2). Maximum nitrification rates were coincident with the NO_2^- maximum at Station 15 and Station 7 (Hurley et al., 2016; rate data were not available for the other two stations; Supplementary Fig. 2). At Station 15 the presence of equatorial upwelling was indicated by high chlorophyll and epipelagic PO_4^{3-} concentrations, as well as a more prominent zone of lower O_2 relative to other sampling stations (Supplementary Fig. 2). Conversely, in the South Atlantic gyre at Station 7, chlorophyll concentration and epipelagic PO_4^{3-} concentration were ca. 4- and 10-fold lower, respectively (Supplementary Fig. 2). Station 23 and Station 2 fell within these productive and oligotrophic end members (Supplementary Fig. 2).

3.2. Depth distribution of GDGT abundance and structures

The depth distribution of GDGTs was generally consistent between size classes and across major GDGT groups: concentration was low in the euphotic zone (< 80 m), reached maximum values near the NO_2^- maximum (75–131 m), decreased between 250 and 350 m, and returned to intermediate values by ca. 500 m (Fig. 2b). Above the NO_2^- maximum, total GDGT concentration ranged from below detection limit to 0.45 ng/l in the small size class (0.3–0.7 μm) and up to 0.49 ng/l in the large size class (0.7–53 μm; Table 3). In and below the NO_2^- maximum, total GDGT concentration ranged from 0.06–2.84 ng/l in the small size class and 0.52–10.3 ng/l in the large size class. At a given depth, 8–67% (avg. 26%) of all GDGTs (summed across both size fractions) were in the small size class, while 33–92% (avg. 76%) were in the large size class. This size class distribution is consistent with work in Hood Canal, Puget Sound, where 36% of total GDGTs were in the 0.2–0.7 μm size class, while 62% were in the 0.7–60 μm size class (Ingalls et al., 2012). The highest maximum GDGT concentration in the large size class (10.3 ng/l) occurred at Station 15, characterized by equatorial upwelling (Table 2), while the lowest was at Station 7 in the South Atlantic Gyre (3.04 ng/l; Table 2).

The most abundant GDGTs in the small and large size classes were IPL-GDGTs with hexose- (1G-GDGTs), dihexose- (2G-GDGTs) and hexose-phosphohexose (HPH-GDGTs) head groups, as well as core GDGTs without polar head groups (Supplementary Fig. 1). The relative proportion of IPL vs. core GDGTs varied with depth and between particle size classes. Water depths above the NO_2^- maximum were characterized by a dominance of core GDGTs and low total GDGT concentration (Fig. 2b–d). Core GDGTs made up 40–98% of total GDGTs above the NO_2^- maximum but only 3–64% at and below the NO_2^- maximum (Table 3). Conversely, IPL-GDGTs made up 2–60% of total GDGTs above the NO_2^- maximum and 36–97% at and below it. In surface waters the small and large size classes contained a similar proportion of IPL-GDGTs; however, at and below the NO_2^- maximum the small size class contained 69–97% IPL-GDGTs while the large class contained only 36–87%. For all stations, when integrated through the water column (0–1000 m), > 98% of total GDGTs were found in waters at and below the NO_2^- maximum.

3.3. TEX_{86} temperature and GDGT [2/3] ratio

TEX_{86} temperature values calculated separately for each GDGT head group (HPH-, 1G-, 2G-GDGTs) and core GDGTs, according to Eq. 2 (Kim et al., 2010), displayed a temperature ordering in which the TEX_{86} temperature of HPH- and 1G-GDGTs was consistently "colder" and more variable than that of core GDGTs (Fig. 2e). In contrast, TEX_{86} temperature of 2G-GDGTs was "warmer" than that of core GDGTs and showed less variability through the water column.

Despite these head group differences, nearly all water column TEX_{86} temperature profiles displayed a common pattern with depth in the upper water column (Fig. 2e). At depths above the NO_2^- maximum, in situ TEX_{86} temperature generally decreased as in situ temperature decreased. TEX_{86} temperature reached a local minimum, or inflection point, at the NO_2^- maximum (ca. 75–130 m) at all stations. Below the NO_2^- maximum at Stations 2, 7 and 15, in situ TEX_{86} values increased between 250 and 350 m (even as in situ temperature continued to fall), before decreasing again below 500 m. This pattern of inflection at ca. 100 m was most evident in the HPH- and 1G-GDGT profiles, but also could be seen to a lesser degree in the 2G- and core GDGT TEX_{86} profiles (Fig. 2e). Thus, the inflection point appeared to be a result of changes in the TEX_{86} ratio *within* each head group class rather than changes in the proportion of the different IPL classes; no systematic varia-

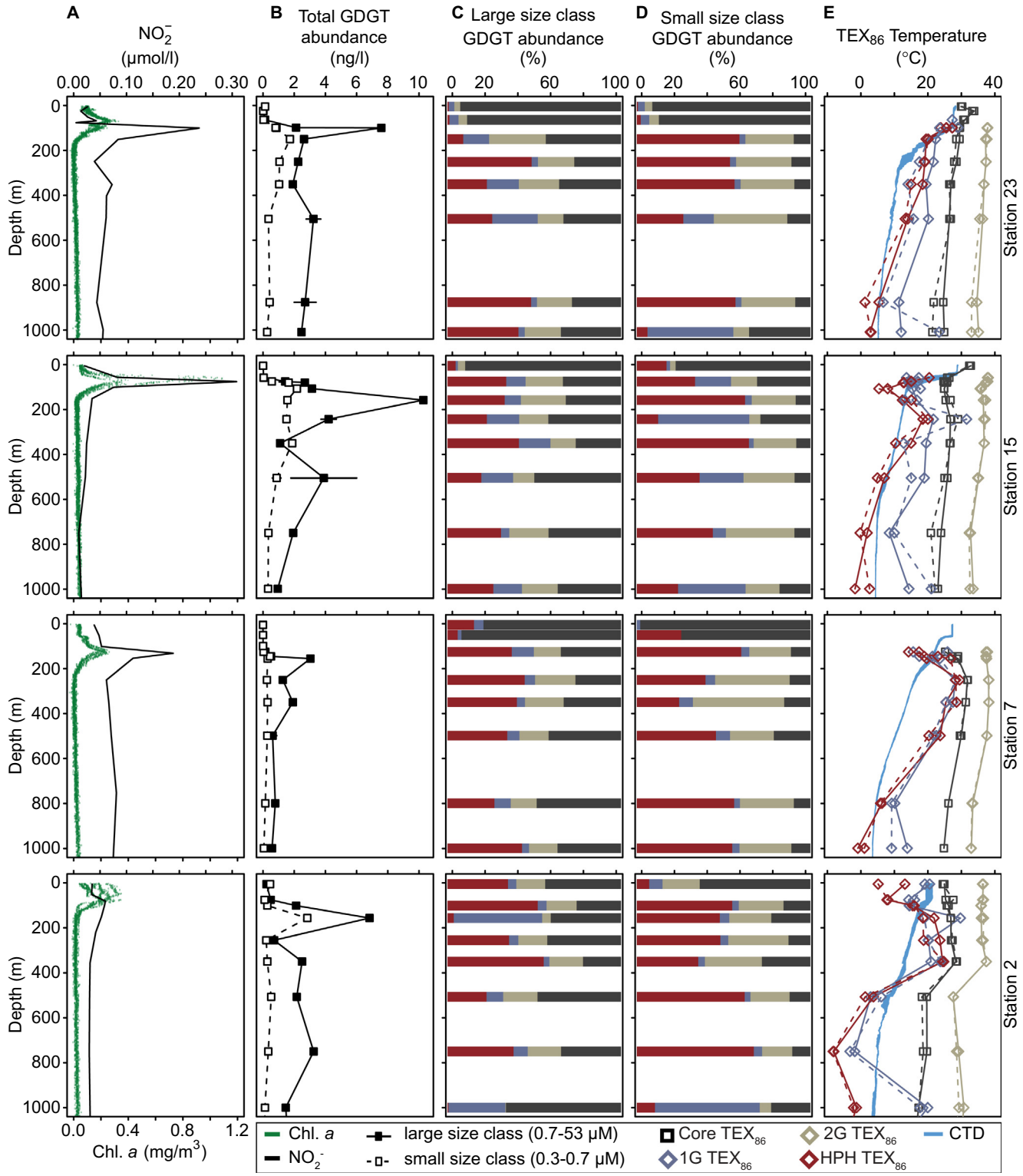

Fig. 2. Hydrocast, GDGT abundance and structural distribution data from SPM at the four sampling stations. A, [NO_2^-] (black) and laboratory-calibrated chlorophyll *a* fluorescence (green). B, total GDGT abundance in the small (0.3–0.7 μm, dashed line) and large (0.7–53 μm, solid line) particle size classes. Error bars represent the concentration range of duplicate filters from the same sampling depth (only available at selected depths). C-D, relative abundance of HPH-GDGTs (red), 1G-GDGTs (blue), 2G-GDGTs (brown), and core GDGTs (black) in the small (C) and large (D) size classes at selected depths (for all depths see Supplementary Fig. 2). E, TEX_{86} temperature of intact polar and core GDGTs in the small (dashed line) and large (solid line) size classes compared with in situ CTD temperature (blue line). (For interpretation of the references to colour in this figure legend, the reader is referred to the web version of this article.)

tion in the relative distribution of head groups was observed through the inflection (Fig. 2c and d).

We summed the GDGTs in the small and large size classes to determine the combined total GDGT concentration, [2/3] ratio, and TEX_{86} at each sampling depth (Fig. 3). The [2/3] ratio from total GDGTs generally increased with depth (Fig. 3e–h, open squares). TEX_{86} values from total GDGTs resembled patterns observed in individual head group classes, with upper water column minima

Table 2
Summary of water column properties and GDGT profile features at each sampling station.

	Deep chlorophyll maximum		SST	NO_2^- maximum		Total GDGT Maximum				TEX_{86} minimum	Export depth estimate[c]	Exported TEX_{86}^c
Station	(mg/m^3)	Depth (m)	(°C)	(μmol/l)	Depth (m)	Small[a] (ng/l)	Depth (m)	Large[b] (ng/l)	Depth (m)	Depth (m)	(m)	(°C)
23	0.32	70	28	0.24	100	1.73	150	7.59	100	150	ca. 100–250	29
15	1.10	60–70	29	0.31	75	2.17	107	10.28	158	107	ca.80–170	23
7	0.27	125	27	0.19	131	0.45	145	3.04	155	145	ca. 135–180	26
2	0.35	50–75	20	0.06	81	2.84	156	6.83	156	75	ca. 90–170	25

[a] 0.3–0.7 μm size fraction; [b] 0.7–53 μm size fraction; [c] from GDGT Export Model 2.

Table 3
Absolute and relative abundances of core GDGTs and intact GDGTs in size-fractionated SPM from each sampling station. Intact GDGTs refers to the sum of 1G-, 2G-, and HPH-GDGTs (b.d., below detection limit, < 0.01 ng/l).

	Station 23		Station 15		Station 7		Station 2		All Stations	
	Small[a]	Large[b]	Small[a]	Large[b]	Small[a]	Large[b]	Small[a]	Large[b]	Small[a]	Large[b]
Absolute Abundance										
Total GDGTs, all depths (ng/l)	0.01–1.73	0.03–4.85	b.d.–2.17	0.01–10.3	b.d.–0.45	b.d.–3.04	0.10–2.84	0.22–68.3	b.d.–2.84	b.d.–10.3
Total GDGTs, surface (ng/l)[c]	0.01–0.13	0.03–0.13	b.d.–0.04	0.01–0.04	b.d.–0.03	b.d.–0.15	0.10–0.45	0.22–0.49	b.d.–0.45	b.d.–0.49
Total GDGTs, sub-surface (ng/l)[d]	0.26–1.73	1.91–4.85	0.33–2.17	0.94–10.3	0.06–0.45	0.52–3.04	0.12–2.84	0.71–6.83	0.06–2.84	0.52–10.3
Relative abundance										
Core GDGTs, all depths (%)	2.67–90.6	22.5–97.0	2.66–76.3	19.9–89.2	4.13–97.9	12.8–91.4	5.09–61.7	17.3–64.3	2.66–97.9	12.8–97.0
Intact GDGTs, all depths (%)	9.43–97.3	3.01–77.5	23.7–97.3	10.8–80.1	2.08–95.9	8.57–87.2	38.3–94.9	35.7–82.7	2.08–97.3	3.01–87.2
Core GDGTs, surface (%)[c]	85.6–90.6	88.1–97.0	42.6–76.3	44.9–89.2	64.0–97.9	70.3–91.4	61.7	40.4	42.6–97.9	40.4–97.0
Intact GDGTs, surface (%)[c]	9.43–14.4	3.01–11.9	23.7–57.4	10.8–55.1	2.08–36.0	8.57–29.7	38.3	59.6	2.08–57.4	3.01–59.6
Core GDGTs, sub-surface (%)[d]	2.67–31.5	22.5–40.0	2.66–26.5	19.9–39.0	4.13–17.4	12.8–45.6	5.09–23.7	17.3–64.3	2.66–31.5	12.8–64.3
Intact GDGTs, sub-surface (%)[d]	68.5–97.3	60.1–77.5	73.5–97.3	61.0–80.1	82.6–95.9	54.4–87.2	76.3–94.9	35.7–82.7	68.5–97.3	35.7–87.2
Total GDGTs by size class (%)	9.64–50.2	49.8–90.4	13.2–63.0	37.0–86.8	8.78–46.3	53.7–91.2	7.88–67.1	32.9–92.1	7.88–67.1	32.9–92.1

[a] 0.3–0.7 μm size fraction; [b] 0.7–53 μm size fraction; [c] depth above the NO_2^- maximum.; [d] depth at or below the NO_2^- maximum.

in TEX_{86} associated with the NO_2^- maximum (Fig. 3i–l, open squares). TEX_{86} temperature from total GDGTs most closely approximated the TEX_{86} temperature from core and 1G-GDGTs, as these two compound classes accounted for a large portion of the total GDGT inventory (Fig. 2c and d). At the NO_2^--associated inflection point, TEX_{86} temperature generally agreed with in situ temperature. Below this depth, in situ temperature decreased, while TEX_{86} temperature was variable but always greater than in situ temperature.

Site-specific details of water column properties and GDGT distributions are provided in the Supplementary material.

4. Discussion

4.1. Patterns in water column GDGT distributions

4.1.1. Correspondence between depth of GDGT production and physiology of Thaumarchaeota

Most archaeal GDGTs reaching marine sediments are believed to be produced by planktonic, ammonia-oxidizing Thaumarchaeota (Schouten et al., 2013). Remineralization of particulate matter sinking out of the euphotic zone (Martin et al., 1987) supplies the NH_4^+ for this reaction. The supply of NH_4^+ decreases exponentially over the upper 1000 m of the water column, which is reflected in the depth distribution of nitrification rate (e.g. Ward, 1987; Ward and Zafiriou, 1988; Beman et al., 2012; Smith et al., 2016). The zonation of remineralization intensity is consistent throughout the global ocean: maximum rates of ammonia oxidation and nitrification occur near the base of the euphotic zone and are frequently marked by a local maximum in NO_2^- concentration (Beman et al., 2012; Newell et al., 2013; Santoro et al., 2013; Hurley et al., 2016; Smith et al., 2016).

At all four of our sampling stations, maximum GDGT concentration occured either coincident with or just below the NO_2^- maximum, between ca. 100 and 200 m (Fig. 2, Table 2). The pattern is similar to the observed vertical distribution of copies of archaeal ammonia monooxygenase (*amoA*) and 16S rRNA genes (Santoro et al., 2010; Beman et al., 2012; Smith et al., 2016). Small vertical offsets between maximum NO_2^- concentration, ammonia oxidation rate, and thaumarchaeal gene copies suggest that additional factors beyond ammonia supply may also regulate the distribution and metabolism of ammonia-oxidizing Thaumarchaeota; however, in general, GDGT abundance and nitrogen remineralization processes appear to be depth correlated.

The low abundance of GDGTs – and particularly of IPL-GDGTs – in surface waters may additionally reflect photic inhibition of Thaumarchaeota (Merbt et al., 2012) or competition with phytoplankton for ammonia. In contrast, throughout the remainder of the sub-photic water column (from the NO_2^- maximum through 1000 m), the proportion of IPL-GDGTs remained high, suggesting that GDGTs may be actively produced throughout the entire upper mesopelagic. This is consistent with low but non-zero mesopelagic nitrification rate (e.g. Santoro et al., 2010).

4.1.2. Depth-dependent variation in TEX_{86}

Although the in situ temperature of the water column decreases with depth, in situ TEX_{86} temperature values did not consistently decrease: TEX_{86} values decreased between surface waters and the NO_2^- maximum, but then increased between the NO_2^- maximum and *ca.* 250–300 m (Fig. 3i–l). TEX_{86} values from SPM deviated from in situ temperature by > 10 °C in the deeper water column. The bidirectional pattern, or NO_2^--associated inflection point in TEX_{86}, is consistent with our recent findings based on continuous culture experiments with the model thaumarchaeon

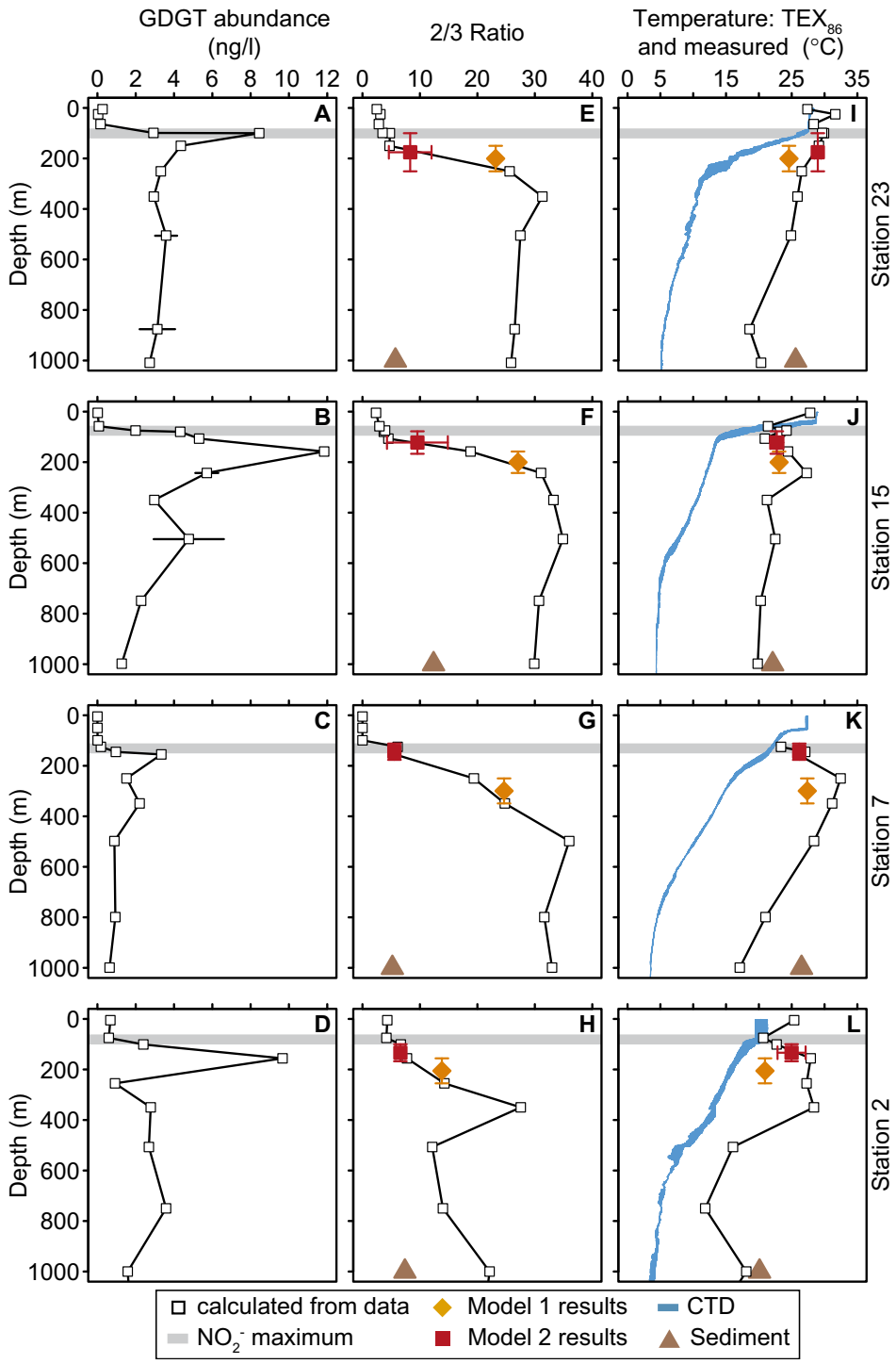

Fig. 3. Total GDGT concentrations and ratios from SPM at the four sampling stations. A–D: Total GDGT concentration in the combined size fraction. Error bars represent the concentration range of duplicate filters from the same sampling depth (only available at selected depths). Column E–H, [2/3] ratio of total GDGTs in combined size fraction (open squares). I–L, TEX_{86} temperature of total GDGTs in combined size fraction (open squares) and in situ CTD temperatures (blue). Gray horizontal bars represent the depth of the NO_2^- maximum. Filled symbols represent the results of GDGT export Model 1 (orange diamonds) and Model 2 (red squares), as well as nearest sediment values (brown triangles). Vertical error bars represent the model-estimated export depth range and horizontal error bars correspond to the range of exported [2/3] ratio or TEX_{86} temperature (see model description in Supplementary Information). (For interpretation of the references to colour in this figure legend, the reader is referred to the web version of this article.)

Nitrosopumilus maritimus SCM1 (Hurley et al., 2016). These experiments showed that TEX_{86} ratios are lower at faster ammonia oxidation rates, resulting in too-cold ("cold-biased") TEX_{86} temperature at faster rates and too-warm TEX_{86} temperature at slower rates.

A dependence on ammonia oxidation rate may also help explain why TEX_{86} ratios sometimes change in the opposite direction of the thermal gradient, and at some stations reach values in the deep subsurface that are "warmer" than the overlying sea surface. In this case, high (warm) TEX_{86} values in the deeper mesopelagic water

column may not reflect sinking, surface-derived SPM, but newly-synthesized lipids at depths where ammonia oxidation rate is low. A dominant contribution from deep mesopelagic GDGTs produced in situ is supported by radiocarbon measurements of GDGTs (Ingalls et al., 2006), as well as the high proportion of IPL-GDGTs and variation in head group patterns between different depths observed here (Fig. 2c and d).

Additional TEX_{86} variability in the mesopelagic below ca. 300 m (e.g. general decrease in TEX_{86} temperature with depth at Station 7 or the TEX_{86} minimum associated with the AAIW at Station 2) suggests that multiple factors in addition to ammonia oxidation rate, including temperature, water mass properties, and thaumarchaeal community composition, may influence TEX_{86} at different depths in the water column. The depth window of GDGT export determines how these various factors affect the TEX_{86} signal preserved in marine sediments.

4.1.3. Depth-dependent variation in [2/3]

The ratio of GDGT-2 to GDGT-3 ([2/3] ratio; Taylor et al., 2013) in SPM generally increases with depth in the water column, potentially providing a unidirectional metric with which to model GDGT export (Fig. 3e–h, open squares). Increasing [2/3] values with depth may be globally ubiquitous (Taylor et al., 2013; Hernández-Sánch ez et al., 2014). The transition from shallow-water to deep-water thaumarchaeal ecotypes has been invoked to explain differences in relative GDGT composition through the water column and may help explain the [2/3] pattern (Villanueva et al., 2015; Kim et al., 2016; Zhu et al., 2016). The average [2/3] value in a global sediment database compiled by Tierney and Tingley (2015) is 6.9 ± 3.1 across locations with water column depth > 500 m.

We identified the sediment locations in the global database nearest to the oceanographic stations studied here to compare water column and sediment GDGT ratios. The sediment locations are 352–941 km from the sampling stations, at Station 15 and Station 23, respectively. The sediments underlie a similar depth of water column (< 500 m difference) at Station 15 and Station 2. However, the sediment water column depth at Stations 7 and 23 is ca. 2000–2400 m shallower than the corresponding oceanographic station.

The sediments nearest to the four oceanographic stations have [2/3] values between 5.2–12.4 (Fig. 3e–h, brown triangles; Table 1). The values resemble our water column [2/3] values at between ca. 100 and 300 m (Supplementary Table 1) and are potentially inconsistent with significant export of GDGTs from deeper in the mesopelagic ocean (> 300 m). The similarity between sediment [2/3] values and the water column [2/3] values in the depth zone of maximum GDGT concentration, as well as the large depth-dependent gradient in [2/3] ratio, suggests it may be possible to use these profiles to better understand GDGT export.

4.2. Modeling GDGT export to sediments

Conceptual explanations for the correlation between sedimentary TEX_{86} ratios and SST have proposed that GDGTs are primarily exported from the surface ocean in association with large sinking aggregates or fecal pellets (Schouten et al., 2002; Wuchter et al., 2006). With improved knowledge of the water column ecology of Thaumarchaeota, and the observed similarity between sedimentary [2/3] values and SPM [2/3] values near the depth of maximum GDGT concentration, we find it natural to explore whether GDGT export instead originates from the areas of the water column where organic matter remineralization and ammonia oxidation rates are highest. We consider two scenarios: one in which GDGTs throughout the upper 1000 m of the water column contribute to export in proportion to their in situ concentration ("GDGT Export Model 1"), and one in which the likelihood of export is weighted toward the upper water column according to conventional understanding of particle aggregation dynamics ("GDGT Export Model 2"). We evaluate these models by comparing the results from our four Western South Atlantic sites to published sedimentary data from nearby locations.

4.2.1. GDGT Export Model 1: Integrated 0–1000 m inventory

In this scenario, we assume that GDGT export to sediments reflects a mass-weighted integral of the upper 1000 m of the water column, effectively assuming that GDGTs at all depths have equal likelihood of being exported. The model uses depth boxes defined by the mid-points between sampling depths and the concentration of total GDGTs in each box, incorporating both the small and large size class. We calculate the [2/3] ratio and the TEX_{86} ratio from GDGTs in each box according to Eqs. 4 and 5, respectively.

$$[2/3]_{\text{depth box}} = \frac{[\text{total GDGTs}]_{\text{small}} \cdot [2/3]_{\text{total GDGTs(small)}} + [\text{total GDGTs}]_{\text{large}} \cdot [2/3]_{\text{total GDGTs(large)}}}{[\text{total GDGTs}]_{\text{small}} + [\text{total GDGTs}]_{\text{large}}} \quad (4)$$

$$[TEX_{86}]_{\text{depth box}} = \frac{[\text{total GDGTs}]_{\text{small}} \cdot [TEX_{86}]_{\text{total GDGTs(small)}} + [\text{total GDGTs}]_{\text{large}} \cdot [TEX_{86}]_{\text{total GDGTs(large)}}}{[\text{total GDGTs}]_{\text{small}} + [\text{total GDGTs}]_{\text{large}}} \quad (5)$$

We then integrate through all depth boxes and determine the [2/3] and TEX_{86} values for GDGTs exported out of the water column (exiting the 1000 m bottom boundary; Supplementary Table 2). To find the average GDGT export depth, we then compare the model-predicted [2/3] value for the exported material to the original water column SPM [2/3] profile (Supplementary Table 1). At Station 23, Model 1 predicts that the [2/3] ratio exported through 1000 m is 23.2, comparable with an average export depth of ca. 250 m (Fig. 3e, orange diamond). Similarly, Model 1 predicts average export depth of ca. 160–240 m at Station 15, ca. 350–500 m at Station 7, and ca. 250–350 m at Station 2 (Fig. 3f–h, respectively, orange diamonds).

The [2/3] values predicted from Model 1 (13.8–27.1) are systematically higher than the global average sedimentary [2/3] value (ca. 6.9 for water columns > 500 m), suggesting that Model 1 may overestimate the mesopelagic contribution of GDGTs. However, it is not trivial to assess if (or to what extent) these differences are significant. SPM represents timescales of weeks or months, while sediment core tops represent 10^1 to 10^3 yr. Lateral transport could also affect sedimentary GDGT distributions, although previous work indicates that GDGTs are more labile than alkenones and are likely to be produced relatively locally (Mollenhauer et al., 2008; Shah et al., 2008). Moreover, GDGT export could be seasonal (e.g. Wuchter et al., 2006), and seasonal variability would not have been captured in our SPM sampling from a single cruise.

Comparison with local sedimentary [2/3] values also suggests that Model 1 overestimates GDGT export depth. The [2/3] values

predicted from Model 1 are higher than the values at the nearest sediment locations (Fig. 3e–h, brown triangles) by more than a factor of 2. The sediment database values would yield inferred export depths ca. 50–275 m shallower than the predictions from Model 1 (Supplementary Table 2), suggesting that Model 1 does not accurately capture the processes leading to GDGT export.

4.2.2. GDGT Export Model 2: Weighted export

In Model 2, we use the same depth-integration structure as Model 1 but refine the model using agreement with [2/3] values in regional sediments. The shallow boundary of estimated export depth is defined as the box containing the NO_2^- maximum, since < 2% of the total GDGT inventory occurs in the boxes above this depth (Supplementary Table 2). Starting at this shallow boundary, we successively incorporate each depth box down the water column until the exported [2/3] value from the model agrees with the sediment [2/3] value (Table 1); the approach predicts an average export depth of GDGTs reaching sediments. The results from Model 2 predict an average export depth of ca. 80–250 m across all stations (Fig. 3e–h, red squares), incorporating only ca. 10–22% of the total water column GDGT inventory (Supplementary Table 2). The depth of GDGT export predicted in Model 2 is ca. 80 m shallower than in Model 1 and is coincident with the maximum in situ GDGT concentration and TEX_{86} minimum at each station (Fig. 3).

The results from Model 2 suggest that export from a layer centered between ca. 80 and 250 m, i.e. the base of the photic zone, is compatible with GDGT ratios from nearby sediments. While GDGTs from this horizon encompass < 25% of the standing stock of GDGTs, the layer may reflect the depth range at which the production of GDGTs best coincides with active aggregation and fecal packaging. In this way, Model 2 appears to reconcile two facts seemingly at odds when the mechanisms by which GDGTs are transported to sediments are considered: Mechanisms that increase the likelihood of incorporation of prokaryotic biomass into sinking flux (e.g. higher particle density, protistan grazing rate and mesoplankton packaging rate) are favored in the surface ocean, yet maximum GDGT concentration occurs deeper where aggregation and packaging are predicted to be less frequent (e.g. McCave, 1984; Jackson and Burd, 1998; Fukuda and Koike, 2004). The results from Model 2 may reflect the intersection of these two processes.

Incorporation of prokaryotic biomass into sinking flux has been addressed extensively, but almost exclusively in the context of surface ocean picoplankton (e.g. Richardson and Jackson, 2007; Close et al., 2013). However, analogies for the potential export of archaeal biomass originating from subsurface waters can be found in low O_2 water columns such as the Cariaco Basin and the Arabian Sea. In these water columns, the rate of chemoautotrophy is very high in upper mesopelagic waters, and the prokaryotic biomass from these depths can be detected in sediment traps (Taylor et al., 2001; Keil et al., 2016). Notably, Wakeham et al. (2003) implicated grazers in the transport of archaeal lipids originating from depths $\leq$ 400 m in the Black Sea to underlying sediments; the lipids of methane-oxidizing archaea residing at depths $\geq$ 700 m were not represented in sinking flux (sediment traps) or sediments, presumably due to the absence of packaging by grazers in methane-rich deep water. Similarly, zooplankton have been implicated elsewhere as consumers of archaeal or chemoautotrophic biomass (e.g. Ingalls et al., 2012; Williams et al., 2014). We suggest that archaeal production occurring in our samples around 80–250 m water depth may be analogously incorporated into sinking flux regardless of the small size of archaeal cells, or may be entrained by deep grazing activity.

Although we did not characterize the GDGT content of particles > 53 μm in diameter, GDGT lipid concentration in this larger size class generally is vanishingly low (Ingalls et al., 2012). It is possible that a high flux of GDGTs could occur from the surface ocean via large sinking particles, although physiological expectations are that thaumarchaeal physiology is not favored in the upper photic zone (e.g. Merbt et al., 2012).

4.3. Effect of modeled GDGT export depth on TEX_{86}

While comparing the results of the GDGT export models with the nearest sediment core-top data introduces spatial and temporal uncertainty, comparison of the two export models provides insight into the export depth sensitivity of TEX_{86}. The [2/3] ratio is highly sensitive to changes in export depth: The exported [2/3] values in Model 1 are on average a factor of 3 higher than the [2/3] values in Model 2, where Model 2 is optimized to agree with sedimentary [2/3] values. In contrast, the exported TEX_{86} signal is nearly the same for both models at Stations 15 and 7 (Fig. 3j and k), and has only a ca. 4 °C difference for Stations 2 and 23 (Fig. 3i and l). The similar TEX_{86} results from both models occur despite very different in situ thermal gradients associated with each scenario. Model 1 integrates depths spanning a gradient of 17 °C on average (between 0 and 1000 m), while Model 2 integrates depths spanning a gradient of 5 °C on average (between the NO_2^- maximum and the optimized base of the export layer). The exported TEX_{86} signal is almost entirely insensitive to these contrasting thermal gradients between the two models, even as the [2/3] ratio changes strongly. Moreover, the ca. 2000–2400 m difference in water column depth between the sediment locations and Stations 7 and 23 does not appear to bias the model results: the predicted export depths from Model 2 correspond to the depth of maximum GDGT concentration across all stations.

Sub-surface export has been invoked to explain bias in TEX_{86} paleotemperature records (e.g. Ho and Laepple, 2016). Yet, the two different depth ranges for modeled export of GDGTs here result in similar values of exported TEX_{86}. We compared the results of the export models with SST measured during sampling (Fig. 3i–l, blue line) and the 20 yr average SST ($OISST_{avg}$) at each sampling station (Table 1) to explore the effect of export depth on exported TEX_{86}-SST agreement. At Stations 7 and 23 the exported TEX_{86} signals in the models generally agree (within 1 °C) with measured SST (Fig. 3i,k; Table 1). At Stations 2 and 15, the offset from SST is greater; this may be a consequence of high ammonia oxidation rate at Station 15 (“cold bias”) and low ammonia oxidation rate at Station 2 (“warm bias”) (Fig. 3j and l). The largest difference between the export model predictions and local SST occurs at Station 15, the location characterized by upwelling, high productivity and intense remineralization. Here, both models predict an exported TEX_{86} signal of ca. 23 °C, 6 °C colder than measured SST (Fig. 3j) and 4 °C colder than $OISST_{avg}$ at that site (Table 1). Since GDGTs are exported from the sub-surface at every station, the “cold bias” at Station 15 represents an additional negative anomaly in TEX_{86}, possibly due to high ammonia oxidation rate. In contrast at Station 2 – where the NO_2^- maximum is least pronounced – the exported TEX_{86} signal in both models overestimates measured SST and $OISST_{avg}$ by ca. 1–7 °C (Fig. 3l; Table 1). The model results suggest that even after determining and accounting for the export depth window, both high productivity and intense remineralization (e.g. Station 15) exert a detectable influence on TEX_{86} which presents as a “cold bias”.

4.4. Comparison with other marine water columns

Our modeling results are consistent with the idea that change in water column TEX_{86} temperature can be explained by the depth-dependent pattern of ammonia oxidation rate, resulting in low TEX_{86} temperature at the NO_2^--maximum and a return to higher

apparent TEX_{86} temperature in deeper waters. Whether this is solely due to changes in archaeal growth rate (Elling et al., 2014; Hurley et al., 2016), or to a succession of specific archaeal taxa optimized to different growth conditions (Sintes et al., 2013; Kim et al., 2016; Smith et al., 2016), remains to be determined. Regardless, the sub-surface in situ TEX_{86} inflection point, i.e. a TEX_{86} minimum followed by deeper TEX_{86} increase, is a feature common to almost all SPM water column profiles measured (*e.g.* Basse et al., 2014; Kim et al., 2016; Turich et al., 2007; Xie et al., 2014; Fig. 4). The occasional absence of this pattern in data sets may be due to lack of sampling in the zone of maximum nitrification (e.g. Schouten et al., 2012) or to other unknown processes (Station 23).

In the Eastern Tropical North Pacific Ocean (ETNP), Xie et al. (2014) observed that water column TEX_{86} temperature for both core and IPL-GDGTs decreased between surface waters and the NO_2^- maximum, and then increased again with depth into the O_2 minimum zone (Fig. 4a). The magnitude of this TEX_{86}-calculated temperature increase is ca. 25 °C for IPL-GDGTs and ca. 13 °C for core GDGTs. Over this same depth range, in situ water column temperature decreased by > 15 °C.

Similarly, in a 4 yr time series off Cape Blanc, NW Africa, Basse et al. (2014) observed TEX_{86} profiles of core GDGTs showing negative inflection points in the upper water column (Fig. 4, B). TEX_{86} temperature decreased with in situ temperature between the surface and depths of ca. 50 m and then increased by up to 10 °C to ca. 200 m, although in situ temperature continued to decrease. In this study, the TEX_{86} profile and the magnitude of the inflection vary between sampling years (2009, 2011 and 2012) despite < 2 °C of in situ temperature change over the same time period. This implies that change in thermal regime cannot be responsible for the change in the TEX_{86} temperature profiles (Fig. 4b).

Finally, along transects off the Portuguese continental margin, Kim et al. (2016) observed TEX_{86} inflection points coincident with the depth of the NO_2^- maximum (Fig. 4c and d). The pattern is apparent in both core and intact polar GDGTs and in both the offshore and more coastal settings (Fig. 4c and d). At the offshore stations, GDGT concentrations are highest at or near the TEX_{86} minimum.

Our model results imply that most sedimentary GDGTs originate from an export layer centered around ca. 80–250 m, the same water column region where TEX_{86} temperature and in situ temperature diverge. The magnitude of the divergence sometimes exceeded 10 °C in the cruise stations reported here, and can be as much as 25 °C across analogous export zones in other regions (e.g. Xie et al., 2014). Therefore, the non-temperature-associated component of TEX_{86} can be much larger than the TEX_{86} calibration

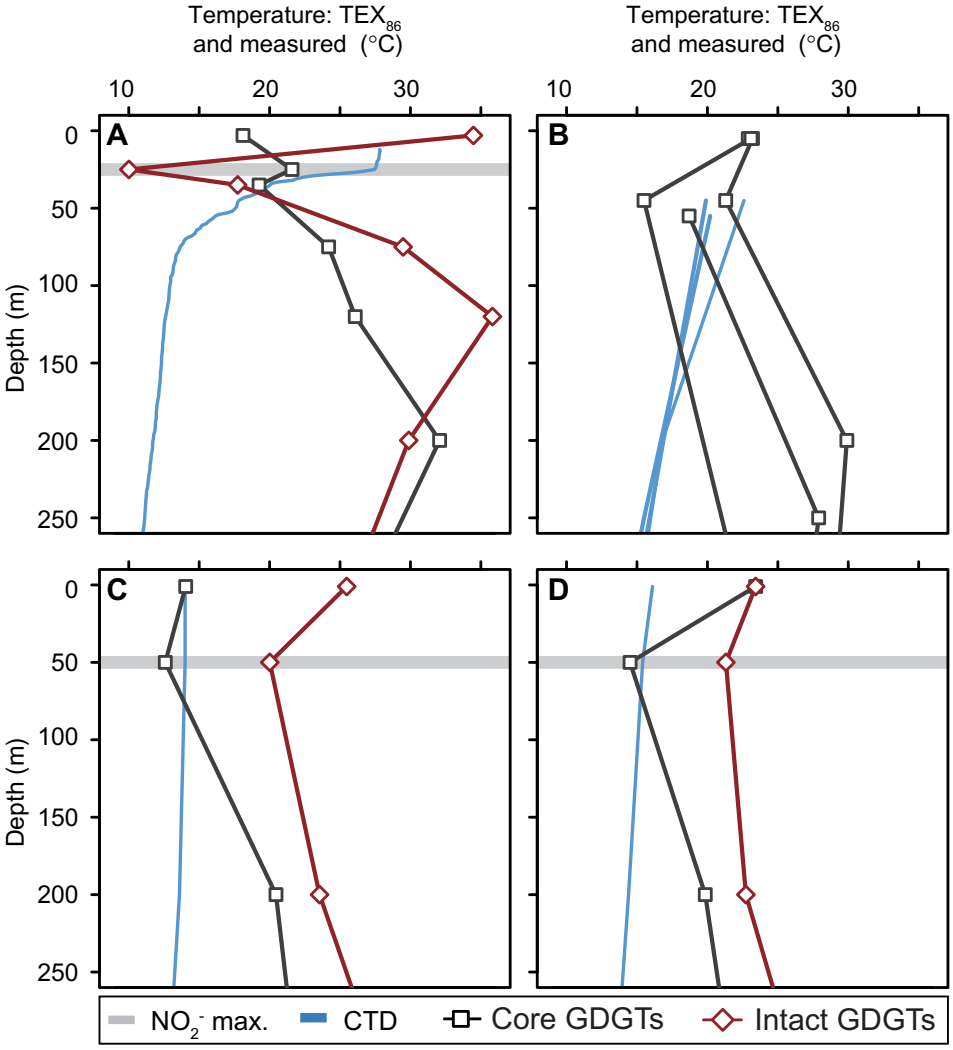

Fig. 4. Partial depth profiles of in situ CTD temperature (blue), and TEX_{86} temperature of core (black squares) and intact polar (red diamonds) GDGTs from published studies. Gray horizontal bars represent depth of NO_2^- maximum. A, Eastern Tropical North Pacific (Xie et al., 2014). B, Cape Blanc, North Atlantic sampled in 2009, 2011, and 2012 (Basse et al., 2014). C and D, Portuguese continental margin, Tagus and Douro transects, respectively; Kim et al., 2016. (For interpretation of the references to colour in this figure legend, the reader is referred to the web version of this article.)

error. Sedimentary TEX_{86} values underlying high productivity, high flux regions appear to be influenced disproportionately by such a non-temperature-associated component. At Station 15, sediment [2/3] and TEX_{86} values agree well with our model of GDGT export from the zone of maximum GDGT concentration. Yet, both exported and sedimentary TEX_{86} ratios under-predict local SST – potentially due to high archaeal ammonia oxidation rate and growth rate. A similar pattern is observed in TEX_{86} temperature for sediments from other nutrient-rich, near shore and upwelling environments (Huguet et al., 2007; Lee et al., 2008; Leider et al., 2010; Rommerskirchen et al., 2011; Wei et al., 2011), supporting a causal link between low TEX_{86} values and increased export productivity and remineralization intensity. Congruently, TEX_{86} temperature in sinking particle studies often shows an inverse relationship with the flux of GDGTs, i.e. high-flux environments show "cold" temperatures (Wuchter et al., 2006; Huguet et al., 2007; Woltering et al., 2012; Yamamoto et al., 2012; Turich et al., 2013; Mollenhauer et al., 2015).

5. Conclusions

At four stations in the Equatorial and Western South Atlantic, the depth distribution of GDGT lipids is consistent with ammonia-oxidizing Thaumarchaeota as the primary source. Maximum GDGT concentration occurs coincident with, or at the base of, the NO_2^- maximum, and > 98% of the integrated GDGT inventory is located below this water column feature. Modeling results suggest that GDGT export from a layer nominally associated with the NO_2^- maximum and just below (80–250 m) is consistent with TEX_{86} and [2/3] values in regional sediments. In this depth zone, TEX_{86} patterns exhibit a complicated relationship with in situ temperature, both correlating and diverging; yet, our models suggest TEX_{86} is uniquely insensitive to the apparent export depth window. Whether integrated down to 1000 m or over a narrower depth window around the NO_2^- maximum, models for exported TEX_{86} still result in proxy values that more closely resemble the surface ocean, rather than in situ temperature. Many water column locations appear to be influenced by the dynamics of organic matter export and remineralization. It is therefore likely that the TEX_{86} values from GDGTs reaching sediments represent a complex interplay between oceanographic variables including – at a minimum – the ocean's thermal properties, nutrient budgets, and archaeal communities. Further research on covariance between TEX_{86}, SST and other oceanographic properties (e.g. global controls on remineralization rate and ammonia oxidation rate) is necessary for better understanding the application of the proxy.

Acknowledgments

We thank F.J. Elling, R.J. Bovee, and S. Shah Walter for providing comments that helped to improve an earlier version of the manuscript, and J. Jennings (Oregon State University) for nutrient analysis. We are grateful to the crew, chief scientists E. Kujawinski and K. Longnecker, and the scientific shipboard part of R/V Knorr cruise KN210-04. Funding for the cruise was provided by the U.S. National Science Foundation (OCE-1154320 to E. Kujawinski and K. Longnecker, WHOI). A.P. and S.J.H. acknowledge funding from the U.S. National Science Foundation (OCE-1129343), the Gordon and Betty Moore Foundation, and the NASA Astrobiology Institute. J.S.L. and K.-U.H. were supported by the Deutsche Forschungsgemeinschaft through the Gottfried Wilhelm Leibniz Program (HI 616-14-1; LC triple quadrupole MS instrument) and by the European Research Council under the European Union's Seventh Framework Programme–"Ideas" Specific Programme, ERC grant agreement No. 247153 (DARCLIFE; PI K.-U.H., funding for: J.S.L.). We also thank B.D.A. Naafs and S.G. Wakeham for constructive reviews.

Appendix A. Supplementary material

Supplementary data associated with this article can be found, in the online version, at https://doi.org/10.1016/j.orggeochem.2017.11.010.

Associate Editor—**C. Turich**

References

Basse, A., Zhu, C., Versteegh, G.J.M., Fischer, G., Hinrichs, K.-U., Mollenhauer, G., 2014. Distribution of intact and core tetraether lipids in water column profiles of suspended particulate matter off Cape Blanc, NW Africa. Organic Geochemistry 72, 1–13.

Beman, M.J., Popp, B.N., Alford, S.E., 2012. Quantification of ammonia oxidation rates and ammonia-oxidizing archaea and bacteria at high resolution in the Gulf of California and eastern tropical North Pacific Ocean. Limnology and Oceanography 57, 711–726.

Brochier-Armanet, C., Boussau, B., Gribaldo, S., Forterre, P., 2008. Mesophilic Crenarchaeota: proposal for a third archaeal phylum, the Thaumarchaeota. Nature reviews. Microbiology 6, 245–252.

Church, M.J., Wai, B., Karl, D.M., DeLong, E.F., 2010. Abundances of crenarchaeal *amoA* genes and transcripts in the Pacific Ocean. Environmental Microbiology 12, 679–688.

Close, H.G., Shah, S.R., Ingalls, A.E., Diefendorf, A.F., Brodie, E.L., Hansman, R.L., Freeman, K.H., Aluwihare, L.I., Pearson, A., 2013. Export of submicron particulate organic matter to mesopelagic depth in an oligotrophic gyre. Proceedings of the National Academy of Sciences 110, 12565–12570.

Elling, F.J., Könneke, M., Lipp, J.S., Becker, K.W., Gagen, E.J., Hinrichs, K.-U., 2014. Effects of growth phase on the membrane lipid composition of the thaumarchaeon *Nitrosopumilus maritimus* and their implications for archaeal lipid distributions in the marine environment. Geochimica et Cosmochimica Acta 141, 579–597.

Elling, F.J., Könneke, M., Mußmann, M., Greve, A., Hinrichs, K.-U., 2015. Influence of temperature, pH, and salinity on membrane lipid composition and TEX_{86} of marine planktonic thaumarchaeal isolates. Geochimica et Cosmochimica Acta 171, 238–255.

Francis, C.A., Roberts, K.J., Beman, J.M., Santoro, A.E., Oakley, B.B., 2005. Ubiquity and diversity of ammonia-oxidizing archaea in water columns and sediments of the ocean. Proceedings of the National Academy of Sciences 102, 14683–14688.

Fukuda, H., Koike, I., 2004. Microbial stimulation of the aggregation process between submicron-sized particles and suspended particles in coastal waters. Aquatic Microbial Ecology 37, 63–73.

Hernández-Sánchez, M.T., Woodward, E.M.S., Taylor, K.W.R., Henderson, G.M., Pancost, R.D., 2014. Variations in GDGT distributions through the water column in the South East Atlantic Ocean. Geochimica et Cosmochimica Acta 132, 337–348.

Ho, S.L., Laepple, T., 2016. Flat meridional temperature gradient in the early Eocene in the subsurface rather than surface ocean. Nature Geoscience 9, 606–610.

Huguet, C., Hopmans, E.C., Febo-Ayala, W., Thompson, D.H., Sinninghe Damsté, J.S., Schouten, S., 2006. An improved method to determine the absolute abundance of glycerol dibiphytanyl glycerol tetraether lipids. Organic Geochemistry 37, 1036–1041.

Huguet, C., Kim, J.-H., Sinninghe Damsté, J.S., Schouten, S., 2006b. Reconstruction of sea surface temperature variations in the Arabian Sea over the last 23 kyr using organic proxies (TEX_{86} and Uk'_{37}). Paleoceanography 21, PA3003.

Huguet, C., Martens-Habbena, W., Urakawa, H., Stahl, D.A., Ingalls, A.E., 2010. Comparison of extraction methods for quantitative analysis of core and intact polar glycerol dialkyl glycerol tetraethers (GDGTs) in environmental samples. Limnology and Oceanography: Methods 8, 127–145.

Huguet, C., Schimmelmann, A., Thunell, R., Lourens, L.J., Sinninghe Damsté, J.S., Schouten, S., 2007. A study of the TEX_{86} paleothermometer in the water column and sediments of the Santa Barbara Basin, California. Paleoceanography 22, PA3203.

Hurley, S.J., Elling, F.J., Könneke, M., Buchwald, C., Wankel, S.D., Santoro, A.E., Lipp, J.S., Hinrichs, K.-U., Pearson, A., 2016. Influence of ammonia oxidation rate on thaumarchaeal lipid composition and the TEX_{86} temperature proxy. Proceedings of the National Academy of Sciences 113, 7762–7767.

Ingalls, A.E., Huguet, C., Truxal, L.T., 2012. Distribution of intact and core membrane lipids of archaeal glycerol dialkyl glycerol tetraethers among size-fractionated particulate organic matter in Hood Canal, Puget Sound. Applied and Environmental Microbiology 78, 1480–1490.

Ingalls, A.E., Shah, S.R., Hansman, R.L., Aluwihare, L.I., Santos, G.M., Druffel, E.R.M., Pearson, A., 2006. Quantifying archaeal community autotrophy in the mesopelagic ocean using natural radiocarbon. Proceedings of the National Academy of Sciences 103, 6442–6447.

Jackson, G.A., Burd, A.B., 1998. Aggregation in the marine environment. Environmental Science & Technology 32, 2805–2814.

Karner, M.B., DeLong, E.F., Karl, D.M., 2001. Archaeal dominance in the mesopelagic zone of the Pacific Ocean. Nature 409, 507–510.

Keil, R.G., Neibauer, J.A., Biladeau, C., van der Elst, K., Devol, A.H., 2016. A multiproxy approach to understanding the "enhanced" flux of organic matter through the oxygen-deficient waters of the Arabian Sea. Biogeosciences 13, 2077–2092.

Kim, J.-H., van der Meer, J., Schouten, S., Helmke, P., Willmott, V., Sangiorgi, F., Koç, N., Hopmans, E.C., Sinninghe Damsté, J.S., 2010. New indices and calibrations derived from the distribution of crenarchaeal isoprenoid tetraether lipids: implications for past sea surface temperature reconstructions. Geochimica et Cosmochimica Acta 74, 4639–4654.

Kim, J.-H., Villanueva, L., Zell, C., Sinninghe Damsté, J.S., 2016. Biological source and provenance of deep-water derived isoprenoid tetraether lipids along the Portuguese continental margin. Geochimica et Cosmochimica Acta 172, 177–204.

Könneke, M., Bernhard, A.E., de la Torre, J.R., Walker, C.B., Waterbury, J.B., Stahl, D.A., 2005. Isolation of an autotrophic ammonia-oxidizing marine archaeon. Nature 437, 543–546.

Kujawinski, E., Longnecker, K., 2013. Inorganic and organic nutrient data from Niskin bottles from R/V Knorr cruise KN210-04 in the Western Atlantic Ocean between Uruguay and Barbados in 2013 (Deep Atlantic DOM project). Biological and Chemical Oceanography Data Management Office (BCO-DMO). Dataset version 2016-07-25. <http://lod.bco-dmo.org/id/dataset/473296> [accessed 2014-08-22].

Kujawinski, E., Longnecker, K.,2014. Processed CTD data from all sensors mounted on the rosette from R/V Knorr cruise KN210-04 in the Western Atlantic Ocean between Uruguay and Barbados in 2013 (Deep Atlantic DOM project). Biological and Chemical Oceanography Data Management Office (BCO-DMO). Dataset version 2014-01-1. <http://lod.bco-dmo.org/id/dataset/481164> [accessed 2014-08-22].

Lee, K.E., Kim, J.-H., Wilke, I., Helmke, P., Schouten, S., 2008. A study of the alkenone, TEX_{86}, and planktonic foraminifera in the Benguela Upwelling System: implications for past sea surface temperature estimates. Geochemistry, Geophysics, Geosystems 9, Q10019.

Leider, A., Hinrichs, K.-U., Mollenhauer, G., Versteegh, G.J.M., 2010. Core-top calibration of the lipid-based $U^{K'}_{37}$ and TEX_{86} temperature proxies on the southern Italian shelf (SW Adriatic Sea, Gulf of Taranto). Earth and Planetary Science Letters 300, 112–124.

Lincoln, S.A., Wai, B., Eppley, J.M., Church, M.J., Summons, R.E., DeLong, E.F., 2014. Planktonic Euryarchaeota are a significant source of archaeal tetraether lipids in the ocean. Proceedings of the National Academy of Sciences 111, 9858–9863.

Martin, J.H., Knauer, G.A., Karl, D.M., Broenkow, W.W., 1987. VERTEX: carbon cycling in the northeast Pacific. Deep-Sea Research 34, 267–285.

Massana, R., Murray, A., Preston, C., DeLong, E., 1997. Vertical distribution and phylogenetic characterization of marine planktonic Archaea in the Santa Barbara Channel. Applied and Environmental Microbiology 63, 50–56.

McCave, I.N., 1984. Size spectra and aggregation of suspended particles in the deep ocean. Deep Sea Research Part A. Oceanographic Research Papers 31, 329–352.

Merbt, S.N., Stahl, D.A., Casamayor, E.O., Martí, E., Nicol, G.W., Prosser, J.I., 2012. Differential photoinhibition of bacterial and archaeal ammonia oxidation. FEMS Microbiology Letters 327, 41–46.

Mollenhauer, G., Basse, A., Kim, J.-H., Sinninghe Damsté, J.S., Fischer, G., 2015. A four-year record of $U^{K'}_{37}$- and TEX_{86}-derived sea surface temperature estimates from sinking particles in the filamentous upwelling region off Cape Blanc, Mauritania. Deep Sea Research Part I: Oceanographic Research Papers 97, 67–79.

Mollenhauer, G., Eglinton, T.I., Hopmans, E.C., Sinninghe Damsté, J.S., 2008. A radiocarbon-based assessment of the preservation characteristics of crenarchaeol and alkenones from continental margin sediments. Organic Geochemistry 39, 1039–1045.

Murray, A., Wu, K., Moyer, C., Karl, D., DeLong, E., 1999. Evidence for circumpolar distribution of planktonic Archaea in the Southern Ocean. Aquatic Microbial Ecology 18, 263–273.

Newell, S.E., Fawcett, S.E., Ward, B.B., 2013. Depth distribution of ammonia oxidation rates and ammonia-oxidizer community composition in the Sargasso Sea. Limnology and Oceanography 58, 1491–1500.

Qin, W., Carlson, L.T., Armbrust, E.V., Devol, A.H., Moffett, J.W., Stahl, D.A., Ingalls, A. E., 2015. Confounding effects of oxygen and temperature on the TEX_{86} signature of marine Thaumarchaeota. Proceedings of the National Academy of Sciences 112, 10979–10984.

Reynolds, R.W., Smith, T.M., Liu, C., Chelton, D.B., Casey, K.S., Schlax, M.G., 2007. Daily high-resolution-blended analyses for sea surface temperature. Journal of Climate 20, 5473–5496.

Richardson, T.L., Jackson, G.A., 2007. Small phytoplankton and carbon export from the surface ocean. Science 315, 838–840.

Rommerskirchen, F., Condon, T., Mollenhauer, G., Dupont, L., Schefuss, E., 2011. Miocene to Pliocene development of surface and subsurface temperatures in the Benguela Current system. Paleoceanography 26, PA3216.

Santoro, A.E., Casciotti, K.L., Francis, C.A., 2010. Activity, abundance and diversity of nitrifying archaea and bacteria in the central California Current. Environmental Microbiology 12, 1989–2006.

Santoro, A.E., Sakamoto, C.M., Smith, J.M., Plant, J.N., Gehman, A.L., Worden, A.Z., Johnson, K.S., Francis, C.A., Casciotti, K.L., 2013. Measurements of nitrite production in and around the primary nitrite maximum in the central California Current. Biogeosciences 10, 7395–7410.

Schouten, S., Forster, A., Panoto, F.E., Sinninghe Damsté, J.S., 2007. Towards calibration of the TEX_{86} palaeothermometer for tropical sea surface temperatures in ancient greenhouse worlds. Organic Geochemistry 38, 1537–1546.

Schouten, S., Hopmans, E.C., Forster, A., van Breugel, Y., Kuypers, M.M.M., Damsté, J.S.S., 2003. Extremely high sea-surface temperatures at low latitudes during the middle Cretaceous as revealed by archaeal membrane lipids. Geology 31, 1069–1072.

Schouten, S., Hopmans, E.C., Schefuß, E., Sinninghe Damsté, J.S., 2002. Distributional variations in marine crenarchaeotal membrane lipids: a new tool for reconstructing ancient sea water temperatures? Earth and Planetary Science Letters 204, 265–274.

Schouten, S., Hopmans, E.C., Sinninghe Damsté, J.S., 2013. The organic geochemistry of glycerol dialkyl glycerol tetraether lipids: a review. Organic Geochemistry 54, 19–61.

Schouten, S., Pitcher, A., Hopmans, E.C., Villanueva, L., van Bleijswijk, J., Sinninghe Damsté, J.S., 2012. Intact polar and core glycerol dibiphytanyl glycerol tetraether lipids in the Arabian Sea oxygen minimum zone: I. Selective preservation and degradation in the water column and consequences for the TEX_{86}. Geochimica et Cosmochimica Acta 98, 228–243.

Shah, S.R., Mollenhauer, G., Ohkouchi, N., Eglinton, T.I., Pearson, A., 2008. Origins of archaeal tetraether lipids in sediments: insights from radiocarbon analysis. Geochimica et Cosmochimica Acta 72, 4577–4594.

Sinninghe Damsté, J.S., 2002. Crenarchaeol: the characteristic core glycerol dibiphytanyl glycerol tetraether membrane lipid of cosmopolitan pelagic crenarchaeota. The Journal of Lipid Research 43, 1641–1651.

Sinninghe Damsté, J.S., Rijpstra, W.I.C., Hopmans, E.C., Prahl, F.G., Wakeham, S.G., Schouten, S., 2002. Distribution of membrane lipids of planktonic crenarchaeota in the Arabian Sea. Applied and Environmental Microbiology 68, 2997–3002.

Sintes, E., Bergauer, K., De Corte, D., Yokokawa, T., Herndl, G.J., 2013. Archaeal amoA gene diversity points to distinct biogeography of ammonia-oxidizing Crenarchaeota in the ocean. Environmental Microbiology 15, 1647–1658.

Smith, J.M., Damashek, J., Chavez, F.P., Francis, C.A., 2016. Factors influencing nitrification rates and the abundance and transcriptional activity of ammonia-oxidizing microorganisms in the dark northeast Pacific Ocean. Limnology and Oceanography 61, 596–609.

Spang, A., Hatzenpichler, R., Brochier-Armanet, C., Rattei, T., Tischler, P., Spieck, E., Streit, W., Stahl, D.A., Wagner, M., Schleper, C., 2010. Distinct gene set in two different lineages of ammonia-oxidizing archaea supports the phylum Thaumarchaeota. Trends in Microbiology 18, 331–340.

Taylor, G.T., Iabichella, M., Ho, T.-Y., Scranton, M.I., Thunell, R.C., Muller-Karger, F., Varela, R., 2001. Chemoautotrophy in the redox transition zone of the Cariaco Basin: a significant midwater source of organic carbon production. Limnology and Oceanography 46, 148–163.

Taylor, K.W.R., Huber, M., Hollis, C.J., Hernandez-Sanchez, M.T., Pancost, R.D., 2013. Re-evaluating modern and Palaeogene GDGT distributions: implications for SST reconstructions. Global and Planetary Change 108, 158–174.

Tierney, J.E., Tingley, M.P., 2014. A Bayesian, spatially-varying calibration model for the TEX_{86} proxy. Geochimica et Cosmochimica Acta 127, 83–106.

Tierney, J.E., Tingley, M.P., 2015. A TEX_{86} surface sediment database and extended Bayesian calibration. Scientific Data 2, 150029.

Turich, C., Freeman, K.H., Bruns, M.A., Conte, M., Jones, A.D., Wakeham, S.G., 2007. Lipids of marine Archaea: patterns and provenance in the water-column and sediments. Geochimica et Cosmochimica Acta 71, 3272–3291.

Turich, C., Schouten, S., Thunell, R.C., Varela, R., Astor, Y., Wakeham, S.G., 2013. Comparison of TEX_{86} and $U^{K'}_{37}$ temperature proxies in sinking particles in the Cariaco Basin. Deep Sea Research Part I: Oceanographic Research Papers 78, 115–133.

Villanueva, L., Schouten, S., Sinninghe Damsté, J.S., 2015. Depth-related distribution of a key gene of the tetraether lipid biosynthetic pathway in marine Thaumarchaeota. Environmental Microbiology 17, 3527–3539.

Wakeham, S.G., Lewis, C.M., Hopmans, E.C., Schouten, S., Sinninghe Damsté, J.S., 2003. Archaea mediate anaerobic oxidation of methane in deep euxinic waters of the Black Sea. Geochimica et Cosmochimica Acta 67, 1359–1374.

Ward, B.B., 1987. Nitrogen transformations in the Southern California Bight. Deep Sea Research Part A. Oceanographic Research Papers 34, 785–805.

Ward, B.B., Zafiriou, O.C., 1988. Nitrification and nitric oxide in the oxygen minimum of the eastern tropical North Pacific. Deep Sea Research Part A. Oceanographic Research Papers 35, 1127–1142.

Wei, Y., Wang, J., Liu, J., Dong, L., Li, L., Wang, H., Wang, P., Zhao, M., Zhang, C.L., 2011. Spatial variations in archaeal lipids of surface water and core-top sediments in the South china sea and their implications for paleoclimate studies. Applied and Environmental Microbiology 77, 7479–7489.

Williams, R.L., Wakeham, S., McKinney, R., Wishner, K.F., 2014. Trophic ecology and vertical patterns of carbon and nitrogen stable isotopes in zooplankton from oxygen minimum zone regions. Deep Sea Research Part I: Oceanographic Research Papers 90, 36–47.

Woltering, M., Werne, J.P., Kish, J.L., Hicks, R., Sinninghe Damsté, J.S., Schouten, S., 2012. Vertical and temporal variability in concentration and distribution of thaumarchaeotal tetraether lipids in Lake Superior and the implications for the application of the TEX_{86} temperature proxy. Geochimica et Cosmochimica Acta 87, 136–153.

Wuchter, C., Schouten, S., Coolen, M.J.L., Sinninghe Damsté, J.S., 2004. Temperature-dependent variation in the distribution of tetraether membrane lipids of marine Crenarchaeota: implications for TEX_{86} paleothermometry. Paleoceanography 19, PA4028.

Wuchter, C., Schouten, S., Wakeham, S.G., Sinninghe Damsté, J.S., 2005. Temporal and spatial variation in tetraether membrane lipids of marine Crenarchaeota in particulate organic matter: implications for TEX_{86} paleothermometry. Paleoceanography 20, PA3013.

Wuchter, C., Schouten, S., Wakeham, S.G., Sinninghe Damsté, J.S., 2006. Archaeal tetraether membrane lipid fluxes in the northeastern Pacific and the Arabian Sea: implications for TEX_{86} paleothermometry. Paleoceanography 21, PA4208.

Xie, S., Liu, X.-L., Schubotz, F., Wakeham, S.G., Hinrichs, K.-U., 2014. Distribution of glycerol ether lipids in the oxygen minimum zone of the Eastern Tropical North Pacific Ocean. Organic Geochemistry 71, 60–71.

Yamamoto, M., Shimamoto, A., Fukuhara, T., Tanaka, Y., Ishizaka, J., 2012. Glycerol dialkyl glycerol tetraethers and TEX_{86} index in sinking particles in the western North Pacific. Organic Geochemistry 53, 52–62.

Zachos, J.C., Schouten, S., Bohaty, S., Quattlebaum, T., Sluijs, A., Brinkhuis, H., Gibbs, S.J., Bralower, T.J., 2006. Extreme warming of mid-latitude coastal ocean during the Paleocene-Eocene Thermal Maximum: inferences from TEX_{86} and isotope data. Geology 34, 737.

Zhu, C., Lipp, J.S., Wörmer, L., Becker, K.W., Schröder, J., Hinrichs, K.-U., 2013. Comprehensive glycerol ether lipid fingerprints through a novel reversed phase liquid chromatography–mass spectrometry protocol. Organic Geochemistry 65, 53–62.

Zhu, C., Wakeham, S.G., Elling, F.J., Basse, A., Mollenhauer, G., Versteegh, G.J.M.M., Könneke, M., Hinrichs, K.-U., 2016. Stratification of archaeal membrane lipids in the ocean and implications for adaptation and chemotaxonomy of planktonic archaea. Environmental Microbiology 18, 4324–4336.